ACS OMEGA

Open Access

http://pubs.acs.org/journal/acsodf

Article

Sensing Hachimoji DNA Bases with Janus MoSH Monolayer Nanodevice: Insights from Density Functional Theory (DFT) and Non-Equilibrium Green's Function Analysis

Vasudeo Babar, Sitansh Sharma,* Abdul Rajjak Shaikh, Romina Oliva, Mohit Chawla, and Luigi Cavallo*

Cite This: *ACS Omega* 2024, 9, 48173−48184

Read Online

ACCESS | Metrics & More | Article Recommendations | Supporting Information

ABSTRACT: Detection of nucleobases is of great significance in DNA sequencing, which is one of the main goals of the Human Genome Project. The synthesis of Hachimoji DNA, an artificial genetic system with eight nucleotide bases, has induced a transformative shift in genetic research and biosensing. Here, we present a systematic investigation of the adsorption behavior and electronic transport properties of natural and modified DNA bases on a Janus molybdenum sulfur hydride (MoSH) monolayer using density functional theory (DFT) and nonequilibrium Green's function (NEGF) methods. Our results demonstrate that the S side of the MoSH monolayer is more effective as a sensing platform compared to the H side, which undergoes significant structural distortions due to chemisorption. The S side selectively distinguishes natural bases A and T from G and C, and modified bases S and Z from others. However, the negligible changes in current after base adsorption highlight the limitations of relying solely on current sensitivity for detection. Our findings provide valuable insights into the design of MoSH monolayer-based sensing platforms for selective DNA base detection, with potential applications in next-generation DNA sequencing technologies.

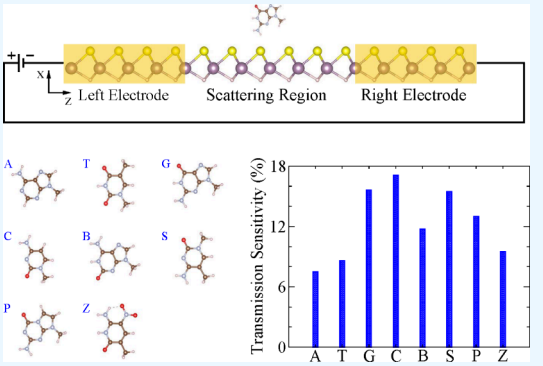

1. INTRODUCTION

Deoxyribonucleic acid (DNA) is the fundamental building block of life, encoding the genetic instructions that govern biological processes across all living organisms.[1,2] Composed of nucleotides—each containing one of four naturally occurring nucleobases linked by a sugar−phosphate backbone—DNA sequences provide the template for protein synthesis and the transmission of genetic information. The rapid advancements in DNA sequencing have catalyzed a new era of precision medicine, presenting significant opportunities to enhance human health.[2] As personalized medicine continues to rise, the demand for sophisticated DNA sensing platforms that enable high-precision sequence analysis has grown. The successful sequencing of the human genome and other species has intensified interest in nucleobase identification.[3] DNA sequencing technology has evolved from the pioneering Sanger method to the latest third-generation techniques, including nanopore/nanogap-based sequencing,[4,5] and chemical and enzymatic methods,[6] pushing the boundaries of DNA analysis. With advancements in bionanoscience, significant efforts have been directed toward developing nanoscale biosensors capable of detecting nucleobases at the single-molecule level.[5] The challenge in nucleobase detection lies in creating sensors that are cost-effective, sensitive, selective, and reliable. Addressing these challenges is essential to fully realize the potential of DNA sequencing in precision medicine, environmental monitoring, genetic disease diagnosis, military counterterrorism, and beyond.[7]

Recent advancements in synthetic biology have led to significant strides in expanding the genetic code of DNA through the development of novel modified nucleotides, extensively investigated for various applications such as precise site-specific labeling and targeted detection probing,[8−11] and structural analysis of nucleic acids.[12−23] In their groundbreaking work, Hoshika et al.[21] integrated modified nucleotides (B, S, P, and Z) with the natural bases (A, T, G, and C) into oligonucleotides, each representing distinct chemical structures, see Figure 1. This innovative approach resulted in the creation of DNA with an expanded eight-base genetic alphabet (A, T, G, C, B, S, P, Z), termed "Hachimoji" DNA, offering significantly enhanced information-storage capacity compared to conventional four-base natural alphabets and previously reported six-base systems.[21,22,24]

This advancement opens new avenues in biomolecular research, offering a broader platform for engineering DNA with

Received: June 8, 2024
Revised: November 14, 2024
Accepted: November 19, 2024
Published: November 26, 2024

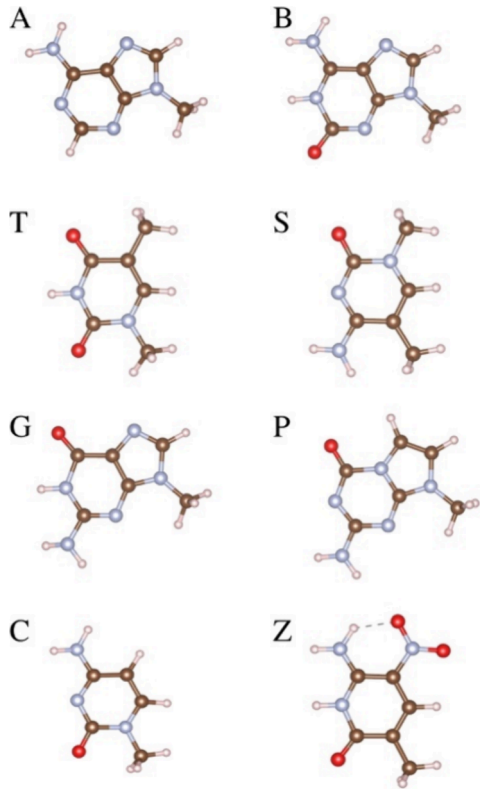

Figure 1. Molecular structures of Hachimoji (A, T, G, C, B, S, P, Z) DNA bases. In the representation, C, N, O, and H atoms are denoted by brown, gray, red, and pink colored spheres, respectively.

customized functionalities that can affect protein synthesis and potentially lead to the creation of novel biomolecules with diverse applications. The incorporation of the modified bases (S, B, Z, P) alongside the traditional natural bases (A, G, C, T) in the Hachimoji DNA molecule has been shown to exhibit structural similarities to canonical DNA when tested within a leukemia virus.[21] Moreover, there is growing interest in exploring the potential therapeutic applications of these bases in treating diseases such as HIV and hepatitis C, highlighting the promising intersection of synthetic biology and medicine. Similar computational investigations on natural and non-natural DNA bases have already been carried for several applications.[25−32]

The experimental validation of unnatural genetic characters presents a significant challenge for label-free next-generation sequencing (NGS) techniques, such as nanopore sensors.[33] While DNA can be driven electrophoretically through nanopores, generating ionic and/or transverse currents that can be detected in real-time, there are still some experimental drawbacks that need to be overcome. These include a low signal-to-noise ratio and too fast translocation speed, which hinder the realization of a label-free, rapid, and low-cost DNA sequencing through solid-state nanopores.[34]

Among the diverse materials available for DNA sensing applications, two-dimensional (2D) materials have garnered significant attention due to their unique electronic and chemical properties.[35−42] Graphene, hexagonal boron nitride (h-BN), graphitic carbon nitride (g-C_3N_4), transition metal dichalcogenides (TMDs) like MoS_2 and WS_2, transition metal oxides (TMOs) such as MoO_3, WO_3, and MnO_2, MXenes, and black phosphorus have all been explored for their potential in biosensing applications.[3,35,36,43−47] In this context, the Janus MoSH monolayer, which was obtained by stripping the top layer S of MoS_2 with H atoms using gentle H_2-plasma treatment at room temperature[48−50] and possessing distinctive composition compared to MoS_2 stands out as a particularly promising candidate for such biosensing applications. Accordingly, this study focuses on elucidating the adsorption behavior and electronic characteristics of Hachimoji DNA on Janus MoSH monolayers, with the aim of advancing our understanding of potential DNA sensing platforms.

Conducting transport measurements on field-effect transistors fabricated from Janus MoSH has revealed a gate voltage-independent and consistently constant carrier concentration, indicating its metallic nature.[50] These findings are further supported by density functional theory (DFT) calculations.[50] Moreover, investigations into phonon-mediated superconductivity have suggested that the light mass and high vibrational frequency of hydrogen impart the Janus MoSH monolayer with robust conventional high-temperature two-dimensional superconducting properties.[51]

The Janus MoSH monolayer shows promise as a metal contact material in high-performance nanodevices, forming a p-type Schottky contact that allows for efficient charge injection.[50] Its electronic structure can be adjusted with external strain and electric fields, enhancing its suitability for optoelectronic applications and demonstrating versatility in heterostructures with other semiconductors.[52−54] Additionally, Janus materials, with their asymmetrical structure and dipole moment, are expected to improve DNA sensing by facilitating stronger dipole−dipole interactions with nucleobases. This capability enhances the sensitivity and selectivity of DNA sensors, making Janus MoSH a valuable candidate for advancing biosensing technologies in genetic research and diagnostics.

The rapid advancement of personalized medicine necessitates the development of innovative sensing technologies for accurate DNA detection. In this study, we investigate the Janus MoSH monolayer as a promising platform for Hachimoji nucleobase sensing in nanodevices. By employing density functional theory and the nonequilibrium Green's function approach, we systematically analyze the interactions between various nucleobases and the MoSH surface. Our goal is to determine key parameters such as binding energy, charge transfer, and the lowest energy configurations, which are critical for optimizing sensor performance. This research not only enhances our understanding of the electronic properties of Hachimoji DNA on Janus MoSH but also contributes to the development of advanced biosensing platforms, ultimately supporting the pursuit of personalized medicine and improved diagnostic capabilities.

2. COMPUTATIONAL DETAILS

The computational study employed first-principles calculations based on density functional theory within the Vienna ab initio simulation package.[55−57] The Perdew−Burke−Ernzerhof (PBE) generalized gradient approximation was utilized for the exchange-correlation potential treatment. Projector-augmented wave potentials were assigned specific valence states: $1s^1$ for H, $2s^22p^2$ for C, $2s^22p^3$ for N, $2s^22p^4$ for O, $3s^23p^4$ for S, and $4p^64d^55s^1$ for Mo.[58] van der Waals interactions were accounted for using the DFT-D3 method.[59] Electronic wave functions were expanded with a plane wave basis set and a 500 eV cutoff energy, with Brillouin zone integrations on 3 × 3 × 1

https://doi.org/10.1021/acsomega.4c05356
ACS Omega 2024, 9, 48173−48184

Monkhorst−Pack k-mesh.[60] Structural optimizations were conducted using the conjugate gradient algorithm until total energy and atomic forces converged below 10^{-6} eV and 5×10^{-3} eV/Å, respectively. The electronic band structure plot is calculated along higher symmetrical k point path from, Gamma (0,0,0), M (1/2,0,0), K (2/3,1/3,0) and Gamma (0,0,0).

For the construction of the two-dimensional material (slab model), a vacuum layer of 16 Å thickness was introduced in the out-of-plane direction. Adsorption studies employed a supercell of dimensions $5 \times 5 \times 1$. The adsorption strength was quantified by the binding energy (E_b), which is defined in eq 1:

$$E_b = E_{\text{monolayer+base}} - (E_{\text{monolayer}} + E_{\text{base}}) \quad (1)$$

where $E_{\text{monolayer+base}}$, $E_{\text{monolayer}}$, and E_{base} are the total energies of the combined system, MoSH monolayer, and base molecule, respectively. The binding energy E_b provides information on the stability of the adsorption between a monolayer and a base molecule. A negative E_b value indicates an exothermic adsorption process, reflecting a favorable base/monolayer structure.

The calculation of current was performed using the nonequilibrium Green's function method, implemented in the TranSIESTA method.[61] The current (I) was defined by the Landauer−Büttiker formula as shown in eq 2

$$I(V) = \frac{2e}{h} \int_{-V/2}^{+V/2} [f_L(E) - f_R(E)] T(E, V) \mathrm{d}E \quad (2)$$

where $f_L(E)$ and $f_R(E)$ are the Fermi distribution functions of the left and right leads, and $T(E, V)$ is the transmission coefficient at energy E and bias voltage V. The $T(E, V)$ is the transmission probability of incoming electron with energy E to get transferred from left electrode to right electrode through central scattering region.

Electronic wave functions were expanded in a polarized double-ζ basis with a 700 Ry cutoff energy. Brillouin zone sampling used $1 \times 5 \times 51$ and $1 \times 5 \times 1$ Monkhorst−Pack k-meshes for lead and transport calculations, respectively. Charge transfers were determined through Bader charge analysis.[62] The charge density difference was calculated using eq 3:

$$\Delta\rho(r) = \rho_{\text{monolayer+base}}(r) - \rho_{\text{monolayer}}(r) - \rho_{\text{base}}(r) \quad (3)$$

where $\Delta\rho(r)$ is derived from the charge density distributions of the combined system ($\rho_{\text{monolayer+base}}$), monolayer ($\rho_{\text{monolayer}}$), and molecule ($\rho_{\text{base}}$). Structures were extracted from the combined system to calculate the charge density distributions of the monolayer and molecule.

To develop a highly efficient DNA base sensor, the primary criterion involves the selective detection of a specific base. The sensitivity of a given monolayer to a particular base molecule is measured by evaluating the change in electronic conductance as well as current compared to the baseline conductance/current (corresponding to the pure monolayer). This evaluation is accomplished using eqs 4 and 5:

$$\text{Transmission Senstivity} = \left| \frac{(G - G_0)}{G_0} \right| \times 100(\%) \quad (4)$$

$$\text{Current Senstivity} = \left| \frac{(I - I_0)}{I_0} \right| \times 100(\%) \quad (5)$$

where G and I represent the electronic conductance (transmission function at 0 V bias) and current flow in the monolayer MoSH based nanodevice after adsorption of particular base, respectively while G_0 and I_0 represent the electronic conductance (transmission function at 0 V bias) and current flow in the pure MoSH monolayer (without base molecules).

3. RESULTS AND DISCUSSION

The optimized atomic structure and electronic band structure for the unit cell of the Janus MoSH monolayer are shown in Figure 2. In the MoSH monolayer, the Mo atom is sandwiched

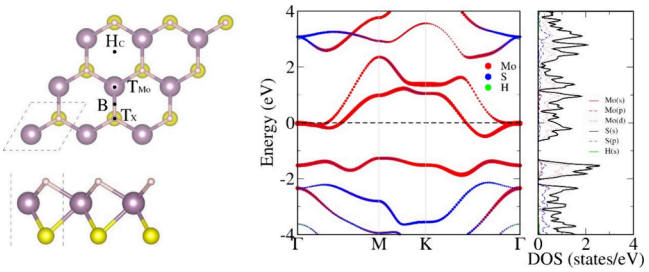

Figure 2. Atomic structure and projected electronic band structure of the hexagonal unit cell in the MoSH monolayer. Mo, S, and H atoms are represented by purple, yellow, and pink spheres, respectively.

between S and H atoms, forming a bond angle (S−Mo−H) of 74.24°. After complete relaxation of the atomic positions along with the lattice parameters, the optimized unit cell of the MoSH monolayer has a lattice constant of $a = b = 2.99$ Å, with Mo−S and Mo−H bond lengths of 2.35 and 2.02 Å, respectively. By measuring the distance between the H atoms and the S atoms, the thickness of the MoSH monolayer is obtained as 2.65 Å. The calculated lattice parameters are in good agreement with earlier experimental[50] and theoretical studies.[48] The projected electronic band structure plot shows the crossing of electronic bands near the Fermi level, which reflects the metallic nature of the monolayer. The electronic bands near the Fermi level have a major contribution from the heavier Mo atom. The projected density of states (PDOS) plots reveal that the bands near the Fermi Level have dominating contribution from the d orbitals of the Mo atom, followed by the p orbitals of the S atom. Interestingly, the s orbitals of the H atoms show no contribution in the valence and conduction bands. Due to the placement of different atoms (H, S) around the Mo atom in the asymmetric atomic structure, the MoSH monolayer generates an intrinsic dipole moment (~0.07 D).

3.1. Adsorption of Hachimoji DNA Bases on MoSH Monolayer. The interactions between natural DNA bases (A, T, G, C) and the modified bases (B, S, P, Z) on the MoSH monolayer are investigated on both the S and H sides. As a first step, the molecular structures of the base molecules and the MoSH monolayer are optimized. In the next step, the center of mass of these molecules is kept at various possible adsorption sites (H_C: hexagonal center, B: bridge, T_{Mo}: top of Mo atom, T_X: top of S or H atom) on the S/H sides of the MoSH monolayer with different orientations, and the lowest energy configurations are obtained (see Figure 2). The binding energies for all different adsorption configurations and their relative energy difference (ΔE) with respect to lowest energy configuration is reported in Table S1.

https://doi.org/10.1021/acsomega.4c05356
ACS Omega 2024, 9, 48173−48184

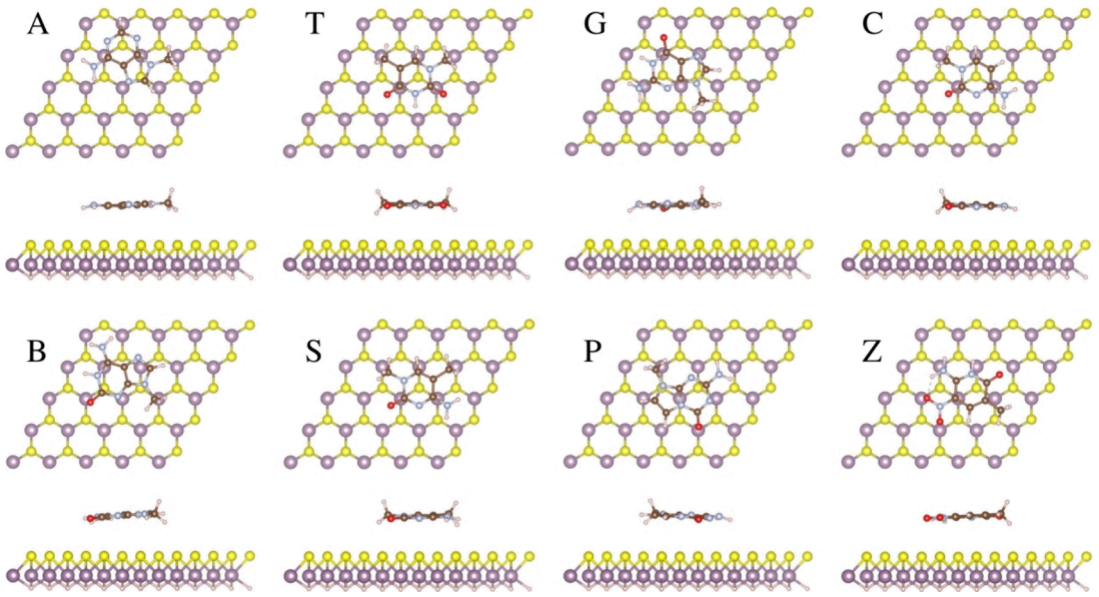

Figure 3. Top and side view of the lowest energy conformations of natural (A, T, G, C) and modified (B, S, P, Z) base molecules on the S side of the MoSH monolayer. Mo, S, H, C, N, and O atoms are represented by purple, yellow, pink, brown, gray, and red spheres, respectively.

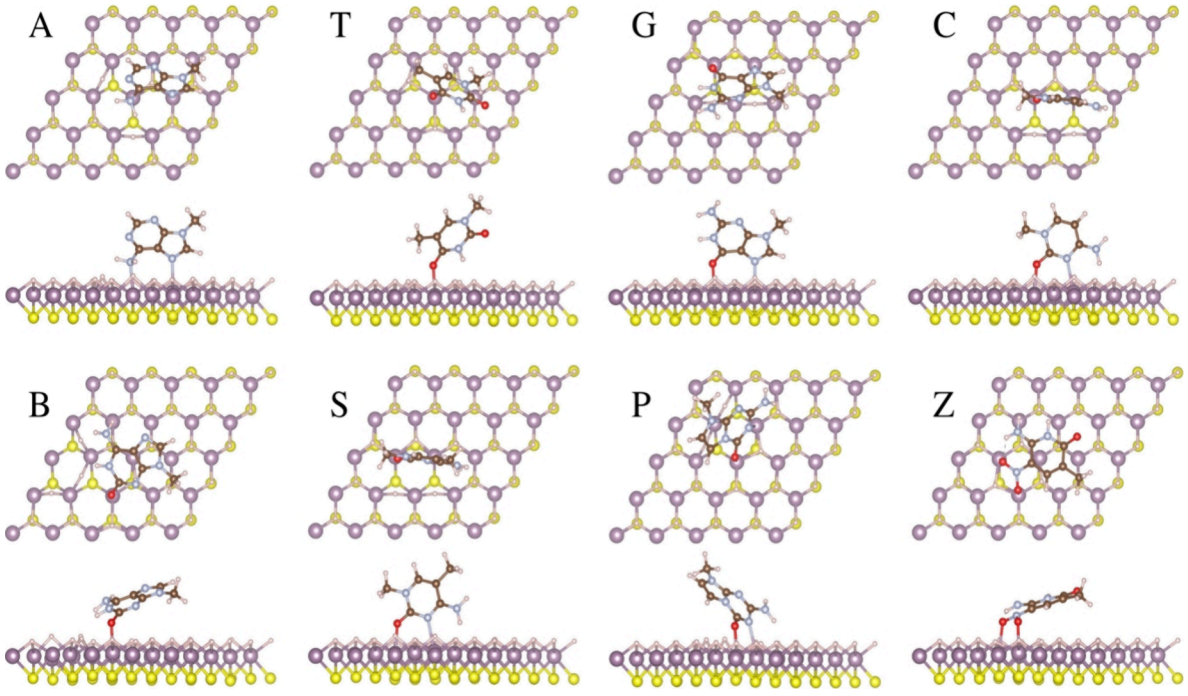

Figure 4. Top and side views of the lowest energy conformations of natural (A, T, G, C) and modified (B, S, P, Z) base molecules on the H side of the MoSH monolayer. Mo, S, H, C, N, and O atoms are depicted by purple, yellow, pink, brown, gray, and red spheres, respectively.

The lowest energy configurations of the natural and modified base molecules on the S and H sides of the MoSH monolayer are shown in Figures 3 and 4, along with the tabulated results in Table 1. For the S side of the MoSH monolayer, all bases prefer a horizontal orientation with respect to the S layer, with the shortest atom-to-atom distance between the monolayer and base molecule within 3.10 Å from the monolayer surface. Additionally, the different bond distances involved in the base molecules as well as the monolayer MoSH show minimum perturbation from their original values.

For S side of MoSH monolayer, among the natural bases, both A and G prefer H_C sites with adsorption energies of −0.843 and −0.981 eV, respectively, while base T and base C prefers the B and T_S sites with an binding energy values of −0.763 and −0.765 eV, respectively. In the case of modified bases, P and Z adsorb on the B site with adsorption energies of −0.910 and −0.886 eV, respectively, while base B and base S prefer H_C and T_S sites with adsorption energies of −0.929 and −0.858 eV, respectively. These binding energy values show that all bases are physisorbed on the S side of the MoSH monolayer, with the maximum binding energy for base G (−0.981 eV) and the minimum binding energy for base T

https://doi.org/10.1021/acsomega.4c05356
ACS Omega 2024, 9, 48173−48184

Table 1. Preferred Adsorption Site, Binding Distance ($D_{h(M-X)}$) (Shortest Atom-to-Atom Distance between Monolayer (M) and Base Molecule (X)), Binding Energy (E_b), and Charge Transfer (ΔQ: ± Sign Indicates Charge Depletion from or Charge Accumulation on Base Molecule) of the Hachimoji Bases Adsorbed on MoSH Monolayer

	MoSH (S side)				MoSH (H side)			
base	site	$D_{h(M-X)}$ (Å)	E_b (eV)	ΔQ (e)	site	$D_{h(M-X)}$ (Å)	E_b (eV)	ΔQ (e)
A	H_C	2.99 (S−H)	−0.843	−0.112	T_H	2.35 (Mo−N)	−1.601	−0.012
T	B	2.92 (S−H)	−0.763	−0.032	T_H	2.15 (Mo−O)	−1.219	0.020
G	H_C	2.87 (S−H)	−0.981	−0.086	T_{Mo}	2.15 (Mo−O)	−2.052	−0.008
C	T_S	2.86 (S−H)	−0.765	−0.057	B	2.13 (Mo−O)	−1.948	−0.007
B	Hc	3.00 (S−H)	−0.929	−0.076	T_{Mo}	2.12 (Mo−O)	−1.859	0.005
S	T_S	2.92 (S−H)	−0.858	−0.072	H_C	2.12 (Mo−O)	−2.014	−0.003
P	B	2.98 (S−H)	−0.910	−0.092	H_C	2.15 (Mo−O)	−1.821	0.000
Z	B	3.10 (S−H)	−0.886	0.437	B	2.22 (Mo−O)	−1.551	0.026

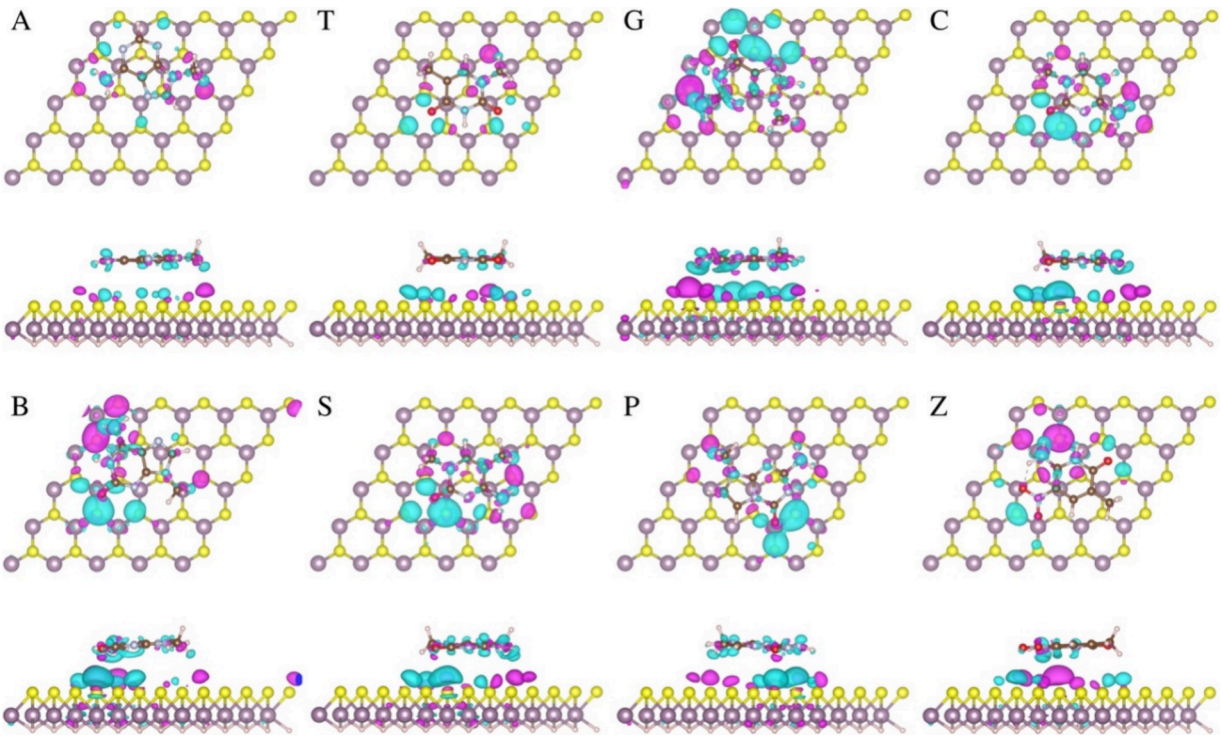

Figure 5. Top and side views of the charge density difference plots for adsorbed natural (A, T, G, C) and modified (B, S, P, Z) base molecules on the S side of Janus MoSH monolayer. Magenta and cyan color isosurfaces represent charge accumulation and depletion, respectively (isosurface value: 5.0×10^{-4} electrons/Å^3). Mo, S, H, C, N, and O atoms are depicted by purple, yellow, pink, brown, gray, and red spheres, respectively.

(−0.763 eV). Among the modified bases, B shows the maximum binding energy of −0.929 eV, while base S shows the least binding energy (−0.858 eV). Overall, the binding energy follows the order: G > B > P > Z > S > A > C > T. Interestingly, the binding energy trend is similar to that obtained for MoS_2 and MoSSe monolayers (S and Se sides) with slightly increased binding energy values.[63]

On the H side of the MoSH monolayer, the base molecules exhibit significantly higher adsorption energies (>−1.2 eV), indicating chemisorption. As a result, the bases prefer a tilted geometry relative to the H layer of the MoSH monolayer. Due to this strong affinity, all bases are in close proximity to the MoSH monolayer surface, with the shortest atom-to-atom distance between the monolayer and base molecule within 2.4 Å. It is observed that the heteroatoms (O and N) present in the base molecules primarily form chemical bonds with the central Mo atom of the monolayer, displacing the lighter hydrogen atoms (see Figure 4). This leads to structural distortion in the monolayer. Similar to the S side, the H side of MoSH also shows maximum (minimum) adsorption for base G (base T). However, the binding energy trend on the H side (G > S > C > B > P > A > Z > T) differs from that observed on the S side. van der Waals and electrostatic interaction analysis is shown in Table S2 shows that for S side of the MoSH monolayer the nature of interaction is mainly van der Waals while in case of H side both the electrostatic and van der Waals interactions have significant contributions.

To gain insight into the interaction between the S/H layer of the MoSH monolayer and the adsorbed base molecules, charge density difference plots are generated and presented in Figures 5 and 6. Figures S1 and S2 illustrate the charge density difference plots for the S- and H-layers of the MoSH monolayer, both represented at a similar isosurface value of 2.75×10^{-3} electrons/Å^3. Upon adsorption on the S side, significant charge redistribution occurs, with the highest charge density typically found between the S layer and the base

https://doi.org/10.1021/acsomega.4c05356
ACS Omega 2024, 9, 48173−48184

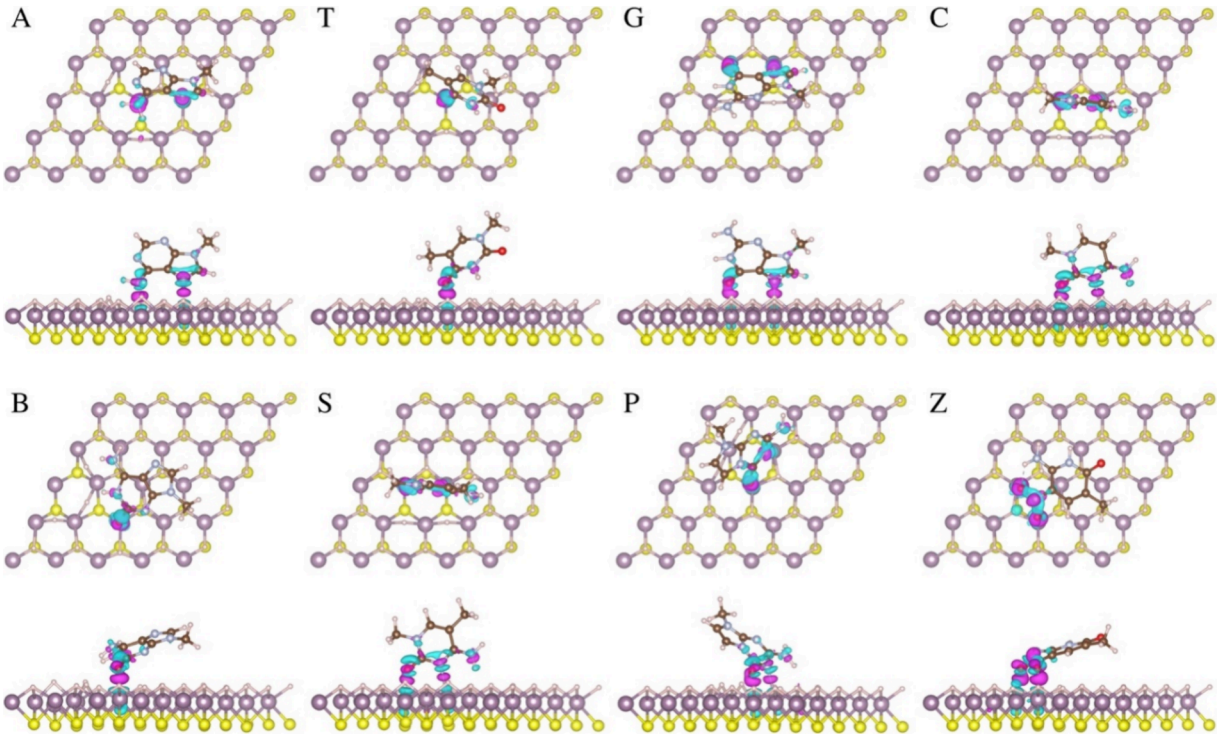

Figure 6. Top and side views of the charge density difference plots for adsorbed natural (A, T, G, C) and modified (B, S, P, Z) base molecules on the H side of Janus MoSH monolayer. Magenta and cyan color isosurfaces represent charge accumulation and depletion, respectively (Isosurface value: 5.0×10^{-3} electrons/Å^3). Mo, S, H, C, N, and O atoms are depicted by purple, yellow, pink, brown, gray, and red spheres, respectively.

molecule (refer to Figure 5). Notably, this charge redistribution correlates with the binding energy, exhibiting more pronounced effects for base G (maximum adsorption) and diminished effects for base T (minimum adsorption). On the H side of the MoSH monolayer, the charge density is predominantly situated between the Mo atom of the monolayer and the heteroatoms (O/N) of the base molecules, confirming the formation of chemical bonds (refer to Figure 6). Looking at the Figure 3, it is clear that the interaction between the lone pair on the sulfur atom in the MoSH monolayer and the nucleobase ring is weakly attractive. This is due to the slightly positive electrostatic potential above the nucleobase's heterocyclic structure.[64] When the dispersion term is added to the PBE functional (specifically, using the PBE-D3), it enhances the stability of this interaction in all cases. Therefore, dispersion interactions are the main factor stabilizing the interaction between the nucleobases and the monolayer. Additionally, electrostatic potential maps show that the slightly positive electrostatic potential on the nucleobase ring[65,66] that causes charge to transfer from the monolayer to the nucleobases. However, in the case of the Z-base, the charge transfer is reversed. This anomaly is likely due to a strong electron-withdrawing group at the C5 position of the Z-base, which instead donates charge to the monolayer.

Quantitative assessment of the charge transfer for both sides of the MoSH monolayer is conducted using Bader charge analysis. The results indicate that on the S side, all bases transfer charges to the monolayer, with the exception of base Z. Conversely, on the H side, depending on the base, a minimal amount of charge is either depleted or accumulated on the MoSH monolayer following base adsorption (see Table 1).

To further characterize the recovery of a clean surface after base adsorption, we analyzed the time spent by each base molecule on the monolayer surface characterized by measuring the translocation time (τ). Using transition state theory, the translocation time (τ) for base molecule on the specific surfaces of Janus MoSH monolayer can be predicted with the relation $\tau = \nu^{-1} e^{(|E_b|/k_B T)}$, where ν is the attempt frequency of bond breaking (1 THz), E_b is the binding energy, k_B is Boltzmann constant and T is temperature (300 K). This relation indicates that base molecules with larger binding energies can remain on the monolayer surface for a longer duration compared to those with smaller binding energies. Due to the significantly higher binding energy values of base molecules on the H side of the MoSH monolayer, their translocation times are substantially longer compared to when they are adsorbed on the S side of MoSH monolayer. For the H side, base G, which has the maximum binding energy, exhibits a translocation time on the order of 2.97×10^{22} s while base T, with the minimum binding energy, shows a translocation time of approximately 2.96×10^{8} s. In comparison, on the S side, base G (which has the maximum binding energy) has a translocation time around 2.99×10^{4} s, while base T (with the minimum binding energy) has a translocation time of only about 6.66 s. These translocation time values lead to the conclusion that due to the formation of chemical bonds between all base molecules and the H side of MoSH, it would take an extremely long time for the adsorbed bases to detach from the scattering region of the nanodevice. Consequently, the bare surface will be unavailable for the next incoming base molecules. On the other hand, the physisorption of bases on the S side of MoSH allows for their easy detachment, making the surface readily available for the next incoming bases in the DNA sequence.

https://doi.org/10.1021/acsomega.4c05356
ACS Omega 2024, 9, 48173−48184

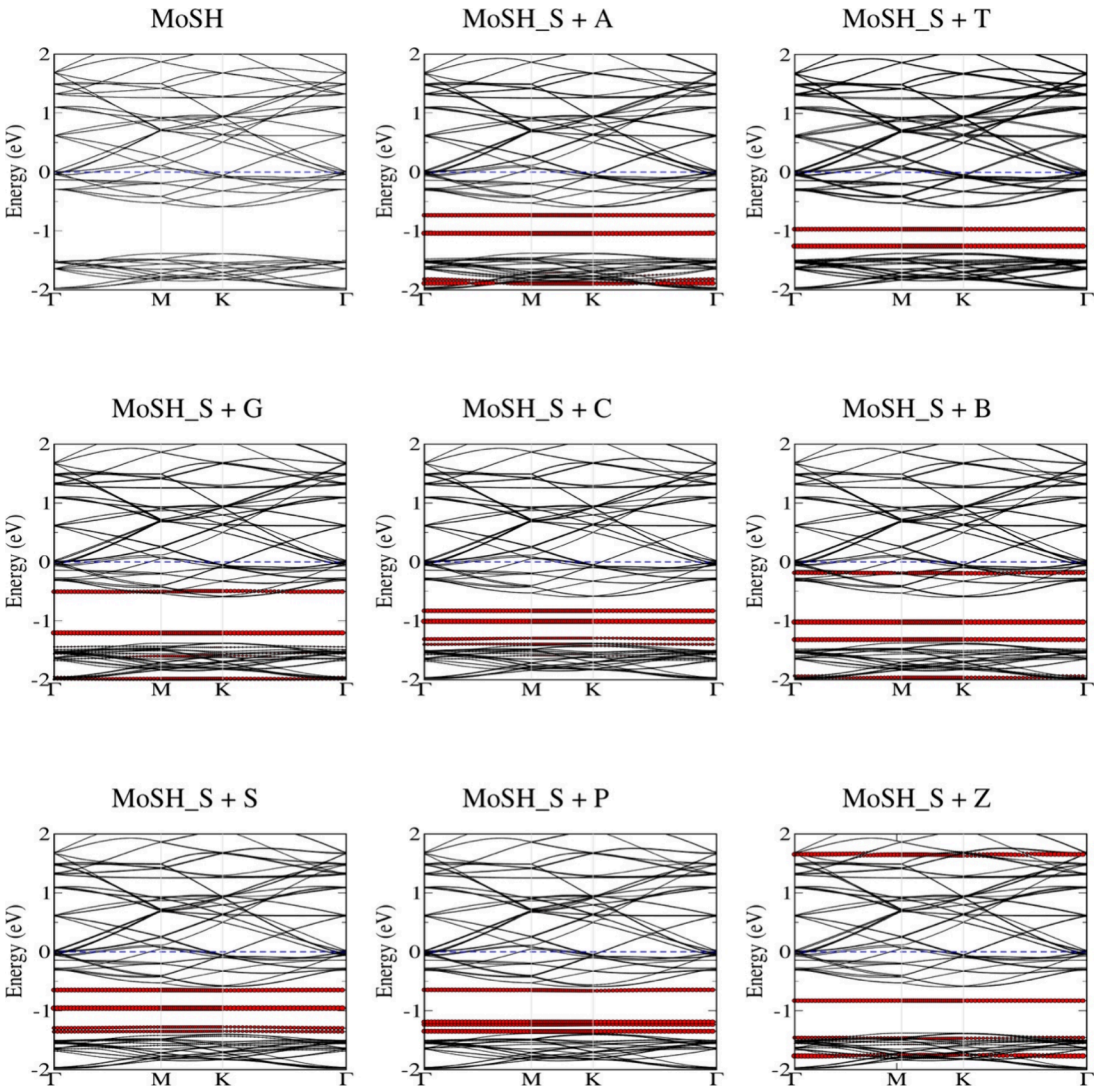

Figure 7. Electronic band structure of pure MoSH monolayer and after base molecule adsorption on the S side of the MoSH monolayer.

3.2. Exploration of Electronic Characteristics. Next, the electronic properties were analyzed using the electronic band structure plots shown in Figure 7 (for the S side of MoSH) and Figure 8 (for the H side of MoSH). The plots reveal that after adsorption of base molecules on the S side of the monolayer, new flat molecular bands are introduced in the electronic band structure of the pure, metallic MoSH monolayer. Interestingly, the electronic band structure features, particularly the band dispersion, show minimal perturbation from the pure MoSH monolayer after base adsorption (see Figure 7). These observations reconfirm the physisorption nature of base molecule adsorption on the S side of the MoSH monolayer.

In contrast, on the H side of the MoSH monolayer, the electronic features (band dispersion) of the band structure exhibit significant deviations from the pure MoSH monolayer after base adsorption. However, the metallic nature of the MoSH monolayer is still retained even after base molecule adsorption on the H side (see Figure 8). This electronic behavior is primarily attributed to the formation of chemical bonds between the base molecules and the H side of the monolayer.

In summary, based on the binding energy values, translocation times (τ), and electronic band structure analysis, we can conclude that the S side of the MoSH monolayer is a superior sensing platform for base molecule detection compared to the H side. The physisorption of base molecules on the S side allows for easy detachment and availability for subsequent sensing, while the chemisorption on the H side leads to prolonged binding times. Additionally, the electronic properties of the S side are minimally perturbed by base adsorption, maintaining the metallic nature of the monolayer. Therefore, only the S side of the MoSH monolayer has been chosen for further electronic transport studies.

3.3. Electronic Transport Studies. The electronic transport properties of a nanodevice composed of a monolayer MoSH are investigated within the framework of the non-equilibrium Green's function approach. The schematic representation of the two-probe nanodevice, with the S side of the MoSH monolayer serving as the sensing platform, is shown in Figure 9a. The setup consists of three parts: the central scattering region (sensing platform) enclosed by semi-infinite left and right electrodes (shaded region). The electronic transport is calculated along the z-direction of the nanodevice, with the central region dimensions of (14.945 Å × 15.531 Å) and both left and right electrodes having dimensions of (14.945 Å × 10.354 Å). To minimize the contact resistance

https://doi.org/10.1021/acsomega.4c05356
ACS Omega 2024, 9, 48173−48184

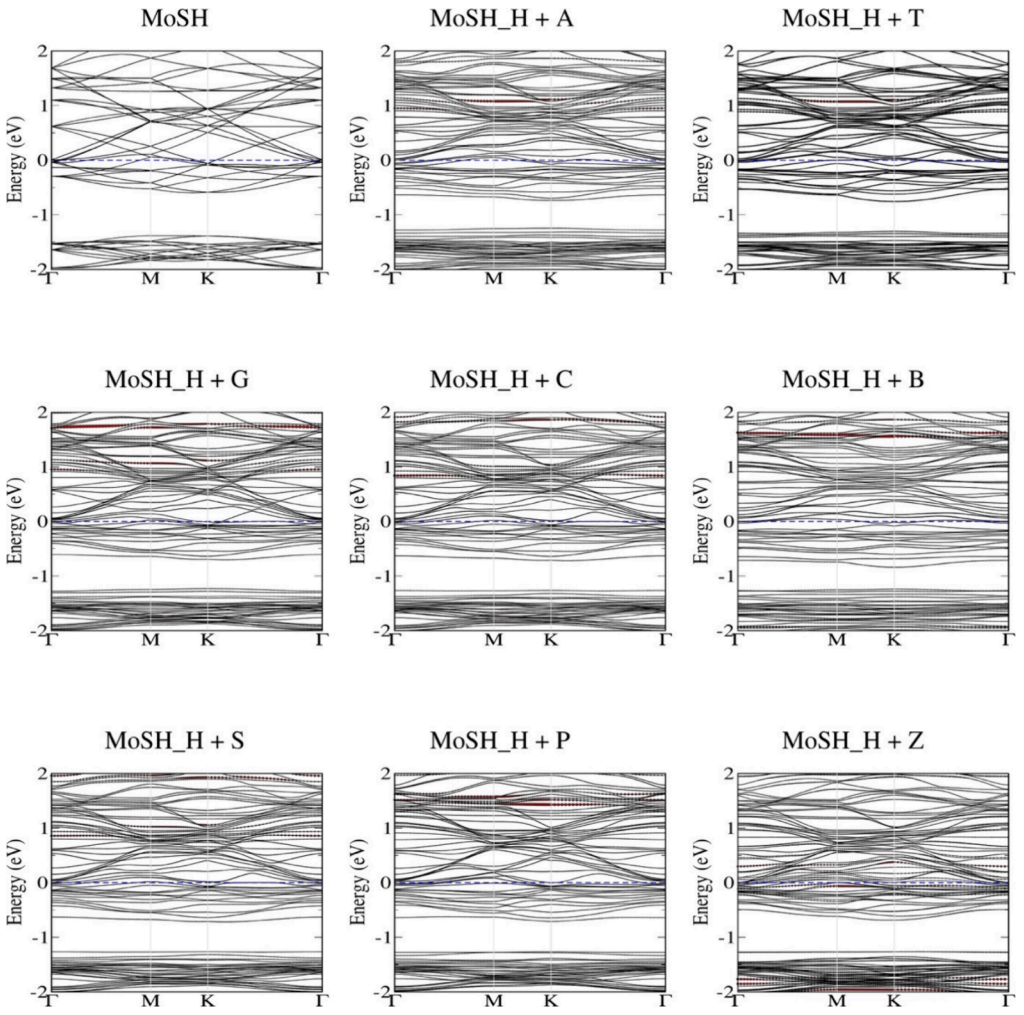

Figure 8. Electronic band structure of pure MoSH monolayer and after base molecule adsorption on the H side of the MoSH monolayer.

between the electrode material and the sensing platform due to the metallic nature of the MoSH monolayer, MoSH is considered as both the electrode and sensing platform material.

The probability of an incoming electron being transferred from the left electrode to the right electrode through the central scattering region is characterized by the energy-resolved transmission spectra $T(E)$ at zero bias voltage. The variation of the transmission function $T(E)$ at zero bias voltage for the pure MoSH monolayer with and without base molecules, with respect to energy in the range of −2 to +2 eV, is shown in Figure 9b. The profile of the transmission function correlates well with the projected band structure plot in Figure 2. Interestingly, the adsorption of base molecules on the MoSH monolayer results in a reduction of the $T(E)$ compared to the pure MoSH monolayer. This suppression in the transmission spectra is due to backscattering, which reduces the conduction channels. Numerous experimental studies have investigated the response of quantized conductance in metallic nanowires to the adsorption of various molecules, including 2,2′-bipyridine, adenine, mercaptopropionic acid, and dopamine, each exhibiting different adsorption strengths. These studies have attributed the observed decrease in conductance to the scattering of conduction electrons caused by the adsorbates.[67−69] The reduction in $T(E)$ values is more pronounced in the energy range of −1.25 to −1.75 eV, especially at −1.46 eV. The comparison of the transmission function $T(E)$ at different bias voltages (0.2, 0.4, and 0.5 V) reveals a decrease in the amplitude of the transmission peak following the adsorption of base molecules, in contrast to the pure MoSH monolayer (see Figure S3). Notably, at bias voltages of 0.2 and 0.4 V, the strongly adsorbed G base exhibits the maximum reduction in the amplitude of the transmission peak, while the weakly adsorbed T base shows the minimum reduction.

To calculate the transmission sensitivity (see eq 4) for different base molecules, the transmission spectra of the pure MoSH monolayer are considered as the reference. Among the natural base molecules, base C shows the maximum transmission sensitivity (17.1%), while base T exhibits the minimum (7.5%). For the modified bases, base S and base Z display the maximum (15.5%) and minimum (9.5%) transmission selectivity, respectively (see Figure 9c). The overall order of transmission sensitivity is C > G ≥ S > P > B > Z > T > A. While natural base molecules A and T can be distinguished from G and C, the low transmission sensitivity resolution may pose a challenge to detect these natural bases individually. However, among the modified base molecules, base S and base Z can be selectively detected, while the signals for base B and base P are almost indistinguishable.

In conclusion, the adsorption of base molecules on the MoSH monolayer leads to a reduction in the transmission function. While the natural base molecules A and T can be distinguished from G and T, the low transmission sensitivity

https://doi.org/10.1021/acsomega.4c05356
ACS Omega 2024, 9, 48173−48184

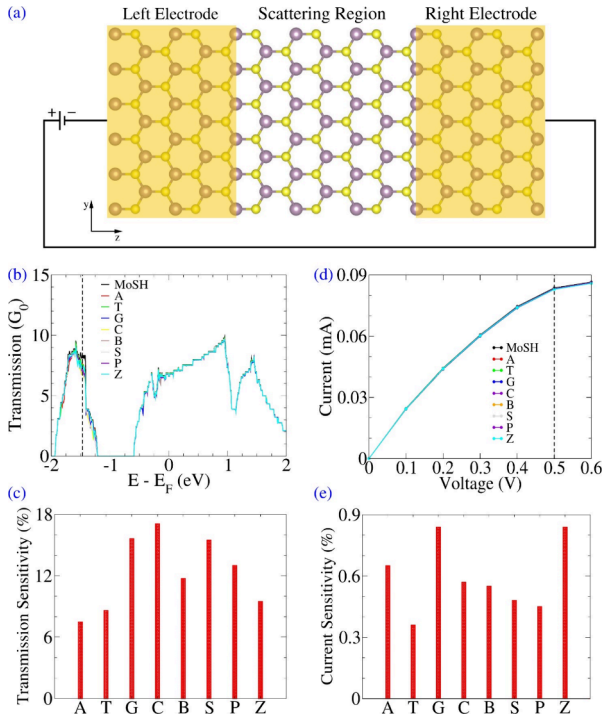

Figure 9. (a) Schematic representation of two-probe nanodevice made up of monolayer MoSH as scattering as well as electrode material, (b) zero-bias transmission spectra for MoSH with and without base molecules, (c) transmission sensitivity histograms at a specific energy value (−1.46 eV), (d) current−voltage characteristics, and (e) current sensitivity at applied voltage of 0.5 V for natural (A, T, G, C) and modified (B, S, P, Z) base molecules on the S side of the MoSH monolayer.

resolution makes the detection of individual natural bases challenging. In contrast, the modified base molecules S and Z can be selectively detected, showcasing the potential of the MoSH monolayer as a versatile sensing platform for DNA sequences presenting Hachimoji DNA bases.

Further, the current−voltage (I−V) characteristics of the pure MoSH monolayer based device with and without base molecules is calculated. The current variation of the proposed device along with the applied voltage ranging from 0 to 0.6 V (step size: 0.1 V) is also shown in Figure 9d. We note that the amount of current flow through the device for pure MoSH monolayer (without base molecule) is of order mA. Interestingly, the adsorption of base molecules on pure MoSH monolayer results in very tiny perturbation in the current as compared to its original values. We believe that this indistinguishable behavior of current is mainly due to metallic nature of the sensing platform, where the adsorption of base molecule is not promising enough to alter the current flow. Similar effect is also reported for DNA base sensing using two probe device made up of metallic borophene nanopore.[70] The metallic behavior of borophene also poses challenges in distinguishing individual nucleotides. Previous studies have shown that applying a higher bias to borophene pore devices may be necessary to detect the four nucleotides individually when they are located inside the pore. However, due to the high computational resource requirements, the researchers were unable to afford a higher bias calculation. Consequently, in the low applied bias window, the current−voltage (I−V) characteristic results for the borophene pore device do not appear promising when compared to the graphene pore device. Hence, graphene continues to be a more suitable material for transverse current-based DNA sequencing applications.[70] Due to very tiny change in the current value after base molecule adsorption the current sensitivity (see eq 5) for the MoSH based device for all studied bases is below 1% (see Figure 9e). Therefore, using the present scenario it would be difficult to detect the natural as well as modified base molecules using the current sensitivity values. We acknowledge that a comprehensive understanding of 2D-material-based DNA sequencing devices necessitates consideration of various factors influencing DNA nucleotide sensing and translocation. Key elements include solvent effects, DNA counterions, structural fluctuations of the 2D monolayer, the chemical properties of the phosphate backbone, and the presence of adjacent nucleotides.[70−72] These factors significantly affect molecular adsorption, binding energy, and transport properties, highlighting the need for future studies to incorporate these variables for a more accurate model of DNA interactions with 2D materials.

As a final remark, we highlight the MoSH nanochannel as a promising alternative to conventional nanopore sequencing techniques. The unique ability of the MoSH nanochannel to detect long DNA strands with controlled orientational fluctuations enhances signal readability, setting it apart from traditional solid-state nanopores and nanogaps.[73] This detection process relies on the adsorption interactions between DNA nucleotides and nanoscale solid-state materials, where changes in electric current provide insights into the molecular composition. However, challenges remain, particularly in the fabrication of ultrathin nanochannels, which restrict their capacity to adsorb and detect only a single molecule at a time. Despite the significant progress in the field, limited experimental studies have been conducted on nanoribbon and nanochannel sequencing, underscoring the need for further theoretical and experimental investigations. We believe that ongoing research will ultimately bridge the gap between nanopore/nanogap technologies and nanochannel-based sequencing, advancing the capabilities of DNA sequencing methodologies.[73]

4. CONCLUSIONS

In this study, we have conducted a systematic investigation of the adsorption and electronic transport properties of the sulfur (S) and hydrogen (H) sides of the MoSH monolayer for Hachimoji bases, utilizing density functional theory in conjunction with the nonequilibrium Green's function approach. Our analysis reveals that all examined bases exhibit physisorption on the S side of the MoSH monolayer, while unexpectedly undergoing chemisorption on the H side, resulting in significant structural distortions within the monolayer.

The evaluation of binding energy, translocation time, and electronic band structure confirms that the S side of the MoSH monolayer is more suitable for detecting base molecules compared to the H side. Additionally, the transmission sensitivity values derived from electronic transport studies underscore the potential of the S side for detecting both natural and modified bases. Notably, among the natural bases, base A and base T can be distinguished from base G and base C, while the modified bases S and Z can be selectively detected.

https://doi.org/10.1021/acsomega.4c05356
ACS Omega 2024, 9, 48173−48184

Overall, the insights gained from this study contribute significantly to the design of MoSH monolayer-based sensing platforms for DNA sequencing applications. The ability to selectively detect natural and modified bases through electronic transport measurements on the S side of the MoSH monolayer positions it as a promising lead candidate for next-generation DNA sequencing technologies.

■ ASSOCIATED CONTENT

Supporting Information

The Supporting Information is available free of charge at https://pubs.acs.org/doi/10.1021/acsomega.4c05356.

Binding energies for various adsorption configurations, a summary of binding energies highlighting the contributions of van der Waals interactions, top and side views of the charge density difference plots for adsorbed base molecules on the S and H sides of the Janus MoSH monolayer, and transmission spectra at different bias voltages (0.2, 0.4, and 0.5 V) for MoSH with and without base molecules (PDF)

■ AUTHOR INFORMATION

Corresponding Authors

Sitansh Sharma − *Department of Research and Innovation, STEMskills Research and Education Lab Private Limited, Faridabad, Haryana 121002, India*;
Email: sitanshsharma@gmail.com

Luigi Cavallo − *Physical Sciences and Engineering Division, Kaust Catalysis Center, King Abdullah University of Science and Technology (KAUST), Thuwal 23955-6900, Saudi Arabia*; orcid.org/0000-0002-1398-338X;
Email: luigi.cavallo@kaust.edu.sa

Authors

Vasudeo Babar − *Physical Sciences and Engineering Division, Kaust Catalysis Center, King Abdullah University of Science and Technology (KAUST), Thuwal 23955-6900, Saudi Arabia*

Abdul Rajjak Shaikh − *Department of Sciences and Technologies, University Parthenope of Naples, Naples 80143, Italy*; orcid.org/0000-0003-4444-0684

Romina Oliva − *Department of Sciences and Technologies, University Parthenope of Naples, Naples 80143, Italy*; orcid.org/0000-0002-6156-6249

Mohit Chawla − *Physical Sciences and Engineering Division, Kaust Catalysis Center, King Abdullah University of Science and Technology (KAUST), Thuwal 23955-6900, Saudi Arabia*; orcid.org/0000-0002-3332-3055

Complete contact information is available at: https://pubs.acs.org/10.1021/acsomega.4c05356

Notes

The authors declare the following competing financial interest(s): S.S. is employed by the company STEMskills Research and Education Lab Private Limited, Faridabad, Haryana, India.

■ ACKNOWLEDGMENTS

The research reported in this publication was supported by funding from King Abdullah University of Science and Technology (KAUST). The Supercomputing Laboratory of KAUST provided computational resources. R.O. and A.R.S. acknowledges support by Ministero dell'Università e della Ricerca (NextGeneration EU PRIN 2022 grant 2022HREZJT).

■ REFERENCES

(1) Berg, J. M.; Tymoczko, J. L.; Stryer, L. *Biochemistry*, 5th edition; W. H. Freeman Publishing: New York, 2002.

(2) Mardis, E. R. A decade's perspective on DNA sequencing technology. *Nature* **2011**, *470* (7333), 198−203.

(3) Tiwari, J. N.; Vij, V.; Kemp, K. C.; Kim, K. S. Engineered Carbon-Nanomaterial-Based Electrochemical Sensors for Biomolecules. *ACS Nano* **2016**, *10* (1), 46−80.

(4) Feng, Y.; Zhang, Y.; Ying, C.; Wang, D.; Du, C. Nanopore-based fourth-generation DNA sequencing technology. *Genomics Proteomics Bioinformatics* **2015**, *13* (1), 4−16.

(5) Ying, Y. L.; Hu, Z. L.; Zhang, S.; Qing, Y.; Fragasso, A.; Maglia, G.; Meller, A.; Bayley, H.; Dekker, C.; Long, Y. T. Nanopore-based technologies beyond DNA sequencing. *Nat. Nanotechnol* **2022**, *17* (11), 1136−1146.

(6) Collins, F. S.; Green, E. D.; Guttmacher, A. E.; Guyer, M. S. A vision for the future of genomics research. *Nature* **2003**, *422* (6934), 835−847.

(7) Nagarajan, V.; Nivedhana, R.; Chandiramouli, R. Nucleobases adsorption studies on chair graphane nanosheets-A DFT outlook. *Inorg. Chem. Commun.* **2023**, *152*, No. 110683.

(8) Hikida, Y.; Kimoto, M.; Yokoyama, S.; Hirao, I. Site-specific fluorescent probing of RNA molecules by unnatural base-pair transcription for local structural conformation analysis. *Nat. Protoc* **2010**, *5* (7), 1312−1323.

(9) Kimoto, M.; Mitsui, T.; Yamashige, R.; Sato, A.; Yokoyama, S.; Hirao, I. A New Unnatural Base Pair System between Fluorophore and Quencher Base Analogues for Nucleic Acid-Based Imaging Technology. *J. Am. Chem. Soc.* **2010**, *132* (43), 15418−15426.

(10) Kimoto, M.; Mitsui, T.; Yokoyama, S.; Hirao, I. A Unique Fluorescent Base Analogue for the Expansion of the Genetic Alphabet. *J. Am. Chem. Soc.* **2010**, *132* (14), 4988−4989.

(11) Sherrill, C. B.; Marshall, D. J.; Moser, M. J.; Larsen, C. A.; Daudé-Snow, L.; Prudent, J. R. Nucleic acid analysis using an expanded genetic alphabet to quench fluorescence. *J. Am. Chem. Soc.* **2004**, *126* (14), 4550−4556.

(12) Kimoto, M.; Endo, M.; Mitsui, T.; Okuni, T.; Hirao, I.; Yokoyama, S. Site-specific incorporation of a photo-crosslinking component into RNA by T7 transcription mediated by unnatural base pairs. *Chem. Biol.* **2004**, *11* (1), 47−55.

(13) Kimoto, M.; Kawai, R.; Mitsui, T.; Yokoyama, S.; Hirao, I. An unnatural base pair system for efficient PCR amplification and functionalization of DNA molecules. *Nucleic Acids Res.* **2009**, *37* (2), No. e14.

(14) Kimoto, M.; Mitsui, T.; Harada, Y.; Sato, A.; Yokoyama, S.; Hirao, I. Fluorescent probing for RNA molecules by an unnatural base-pair system. *Nucleic Acids Res.* **2007**, *35* (16), 5360−5369.

(15) Flamme, M.; Röthlisberger, P.; Levi-Acobas, F.; Chawla, M.; Oliva, R.; Cavallo, L.; Gasser, G.; Marlière, P.; Herdewijn, P.; Hollenstein, M. Enzymatic Formation of an Artificial Base Pair Using a Modified Purine Nucleoside Triphosphate. *ACS Chem. Biol.* **2020**, *15* (11), 2872−2884.

(16) Chawla, M.; Poater, A.; Besalú-Sala, P.; Kalra, K.; Oliva, R.; Cavallo, L. Theoretical characterization of sulfur-to-selenium substitution in an emissive RNA alphabet: impact on H-bonding potential and photophysical properties. *Phys. Chem. Chem. Phys.* **2018**, *20* (11), 7676−7685.

(17) Chawla, M.; Poater, A.; Oliva, R.; Cavallo, L. Structural and energetic characterization of the emissive RNA alphabet based on the isothiazolo[4,3-d]pyrimidine heterocycle core. *Phys. Chem. Chem. Phys.* **2016**, *18* (27), 18045−18053.

(18) Chawla, M.; Credendino, R.; Oliva, R.; Cavallo, L. Structural and Energetic Impact of Non-Natural 7-Deaza-8-Azaadenine and Its

7-Substituted Derivatives on H-Bonding Potential with Uracil in RNA Molecules. *J. Phys. Chem. B* **2015**, *119* (41), 12982−12989.
(19) Chawla, M.; Gorle, S.; Shaikh, A. R.; Oliva, R.; Cavallo, L. Replacing thymine with a strongly pairing fifth Base: A combined quantum mechanics and molecular dynamics study. *Comput. Struct Biotec* **2021**, *19*, 1312−1324.
(20) Chawla, M.; Minenkoy, Y.; Vu, K. B.; Oliva, R.; Cavallo, L. Structural and Energetic Impact of Non-natural 7-Deaza-8-azaguanine, 7-Deaza-8-azaisoguanine, and Their 7-Substituted Derivatives on Hydrogen-Bond Pairing with Cytosine and Isocytosine. *ChemBioChem* **2019**, *20* (17), 2262−2270.
(21) Hoshika, S.; Leal, N. A.; Kim, M. J.; Kim, M. S.; Karalkar, N. B.; Kim, H. J.; Bates, A. M.; Watkins, N. E., Jr.; SantaLucia, H. A.; Meyer, A. J.; DasGupta, S.; Piccirilli, J. A.; Ellington, A. D.; SantaLucia, J., Jr.; Georgiadis, M. M.; Benner, S. A. Hachimoji DNA and RNA: A genetic system with eight building blocks. *Science* **2019**, *363* (6429), 884−887.
(22) Dhami, K.; Malyshev, D. A.; Ordoukhanian, P.; Kubelka, T.; Hocek, M.; Romesberg, F. E. Systematic exploration of a class of hydrophobic unnatural base pairs yields multiple new candidates for the expansion of the genetic alphabet. *Nucleic Acids Res.* **2014**, *42* (16), 10235−10244.
(23) Chawla, M.; Poater, A.; Oliva, R.; Cavallo, L. Unveiling Structural and Energetic Characterization of the Emissive RNA Alphabet Anchored in the Methylthieno[3,4-d]pyrimidine Heterocycle Core. *Phys. Chem. Chem. Phys.* **2024**, *26*, 16358−16368.
(24) Malyshev, D. A.; Dhami, K.; Lavergne, T.; Chen, T.; Dai, N.; Foster, J. M.; Correa, I. R., Jr.; Romesberg, F. E. A semi-synthetic organism with an expanded genetic alphabet. *Nature* **2014**, *509* (7500), 385−388.
(25) de Souza, F. A. L.; Sivaraman, G.; Fyta, M.; Scheicher, R. H.; Scopel, W. L.; Amorim, R. G. Electrically sensing Hachimoji DNA nucleotides through a hybrid graphene/-BN nanopore. *Nanoscale* **2020**, *12* (35), 18289−18295.
(26) Prasongkit, J.; Grigoriev, A.; Pathak, B.; Ahuja, R.; Scheicher, R. H. Transverse Conductance of DNA Nucleotides in a Graphene Nanogap from First Principles. *Nano Lett.* **2011**, *11* (5), 1941−1945.
(27) Prasongkit, J.; Grigoriev, A.; Pathak, B.; Ahuja, R.; Scheicher, R. H. Theoretical Study of Electronic Transport through DNA Nucleotides in a Double-Functionalized Graphene Nanogap. *J. Phys. Chem. C* **2013**, *117* (29), 15421−15428.
(28) Pathak, B.; Löfås, H.; Prasongkit, J.; Grigoriev, A.; Ahuja, R.; Scheicher, R. H. Double-functionalized nanopore-embedded gold electrodes for rapid DNA sequencing. *Appl. Phys. Lett.* **2012**, *100* (2), No. 023701.
(29) Min, S. K.; Kim, W. Y.; Cho, Y.; Kim, K. S. Fast DNA sequencing with a graphene-based nanochannel device. *Nat. Nanotechnol* **2011**, *6* (3), 162−165.
(30) Lee, J. H.; Choi, Y. K.; Kim, H. J.; Scheicher, R. H.; Cho, J. H. Physisorption of DNA Nucleobases on -BN and Graphene: vdW-Corrected DFT Calculations. *J. Phys. Chem. C* **2013**, *117* (26), 13435−13441.
(31) Shukla, V.; Jena, N. K.; Grigoriev, A.; Ahuja, R. Prospects of Graphene-hBN Heterostructure Nanogap for DNA Sequencing. *Acs Appl. Mater. Inter* **2017**, *9* (46), 39945−39952.
(32) Prasongkit, J.; Jungthawan, S.; Amorim, R. G.; Scheicher, R. H. Single-molecule DNA sequencing using two-dimensional TiC(OH) MXene nanopores: A first-principles investigation. *Nano Res.* **2022**, *15* (11), 9843−9849.
(33) Branton, D.; Deamer, D. W.; Marziali, A.; Bayley, H.; Benner, S. A.; Butler, T.; Di Ventra, M.; Garaj, S.; Hibbs, A.; Huang, X.; Jovanovich, S. B.; Krstic, P. S.; Lindsay, S.; Ling, X. S.; Mastrangelo, C. H.; Meller, A.; Oliver, J. S.; Pershin, Y. V.; Ramsey, J. M.; Riehn, R.; Soni, G. V.; Tabard-Cossa, V.; Wanunu, M.; Wiggin, M.; Schloss, J. A. The potential and challenges of nanopore sequencing. *Nat. Biotechnol.* **2008**, *26* (10), 1146−1153.
(34) Fyta, M. Threading DNA through nanopores for biosensing applications. *J. Phys.: Condens. Mater.* **2015**, *27* (27), No. 273101.
(35) Novoselov, K. S.; Geim, A. K.; Morozov, S. V.; Jiang, D.; Zhang, Y.; Dubonos, S. V.; Grigorieva, I. V.; Firsov, A. A. Electric field effect in atomically thin carbon films. *Science* **2004**, *306* (5696), 666−669.
(36) Zhang, H. Ultrathin Two-Dimensional Nanomaterials. *ACS Nano* **2015**, *9* (10), 9451−9469.
(37) Jariwala, D.; Marks, T. J.; Hersam, M. C. Mixed-dimensional van der Waals heterostructures. *Nat. Mater.* **2017**, *16* (2), 170−181.
(38) Chen, D.; Jiang, J.; Weatherley, T. F. K.; Carlin, J. F.; Banerjee, M.; Grandjean, N. GaN Surface Passivation by MoS(2) Coating. *Nano Lett.* **2024**, *24* (33), 10124−10130.
(39) Boyd, J. A.; Cao, Z. L.; Yadav, P.; Farimani, A. B. DNA Detection Using a Single-Layer Phosphorene Nanopore. *ACS Appl. Nano Mater.* **2023**, *6* (9), 7814−7820.
(40) Zhu, C. Z.; Du, D.; Lin, Y. H. Graphene and graphene-like 2D materials for optical biosensing and bioimaging: a review. *2D Mater.* **2015**, *2* (3), No. 032004.
(41) Georgakilas, V.; Tiwari, J. N.; Kemp, K. C.; Perman, J. A.; Bourlinos, A. B.; Kim, K. S.; Zboril, R. Noncovalent Functionalization of Graphene and Graphene Oxide for Energy Materials, Biosensing, Catalytic, and Biomedical Applications. *Chem. Rev.* **2016**, *116* (9), 5464−5519.
(42) Qiu, H.; Zhou, W. Q.; Guo, W. L. Nanopores in Graphene and Other 2D Materials: A Decade's Journey toward Sequencing. *ACS Nano* **2021**, *15* (12), 18848−18864.
(43) Hu, Y. L.; Huang, Y.; Tan, C. L.; Zhang, X.; Lu, Q. P.; Sindoro, M.; Huang, X.; Huang, W.; Wang, L. H.; Zhang, H. Two-dimensional transition metal dichalcogenide nanomaterials for biosensing applications. *Mater. Chem. Front* **2017**, *1* (1), 24−36.
(44) Su, S.; Sun, Q.; Gu, X. D.; Xu, Y. Q.; Shen, J. L.; Zhu, D.; Chao, J.; Fan, C. H.; Wang, L. H. Two-dimensional nanomaterials for biosensing applications. *Trac, Trends Anal. Chem.* **2019**, *119*, 115610.
(45) Tan, C.; Cao, X.; Wu, X. J.; He, Q.; Yang, J.; Zhang, X.; Chen, J.; Zhao, W.; Han, S.; Nam, G. H.; Sindoro, M.; Zhang, H. Recent Advances in Ultrathin Two-Dimensional Nanomaterials. *Chem. Rev.* **2017**, *117* (9), 6225−6331.
(46) Xu, M.; Liang, T.; Shi, M.; Chen, H. Graphene-like two-dimensional materials. *Chem. Rev.* **2013**, *113* (5), 3766−3798.
(47) Li, L.; Yu, Y.; Ye, G. J.; Ge, Q.; Ou, X.; Wu, H.; Feng, D.; Chen, X. H.; Zhang, Y. Black phosphorus field-effect transistors. *Nat. Nanotechnol* **2014**, *9* (5), 372−377.
(48) Lu, A. Y.; Zhu, H. Y.; Xiao, J.; Chuu, C. P.; Han, Y. M.; Chiu, M. H.; Cheng, C. C.; Yang, C. W.; Wei, K. H.; Yang, Y. M.; Wang, Y.; Sokaras, D.; Nordlund, D.; Yang, P. D.; Muller, D. A.; Chou, M. Y.; Zhang, X.; Li, L. J. Janus monolayers of transition metal dichalcogenides. *Nat. Nanotechnol.* **2017**, *12* (8), 744−749.
(49) Rangel, A. E.; Hariri, A. A.; Eisenstein, M.; Soh, H. T. Engineering Aptamer Switches for Multifunctional Stimulus-Responsive Nanosystems. *Adv. Mater.* **2020**, *32* (50), No. e2003704.
(50) Wan, X.; Chen, E.; Yao, J.; Gao, M.; Miao, X.; Wang, S.; Gu, Y.; Xiao, S.; Zhan, R.; Chen, K.; Chen, Z.; Zeng, X.; Gu, X.; Xu, J. Synthesis and Characterization of Metallic Janus MoSH Monolayer. *ACS Nano* **2021**, *15* (12), 20319−20331.
(51) Liu, P. F.; Zheng, F. P.; Li, J. Y.; Si, J. G.; Wei, L. M.; Zhang, J. R.; Wang, B. T. Two-gap superconductivity in a Janus MoSH monolayer. *Phys. Rev. B* **2022**, *105* (24), No. 245420.
(52) Nguyen, C. V.; Nguyen, C. Q.; Nguyen, S. T.; Ang, Y. S.; Hieu, N. V. Two-Dimensional Metal/Semiconductor Contact in a Janus MoSH/MoSiN van der Waals Heterostructure. *J. Phys. Chem. Lett.* **2022**, *13* (11), 2576−2582.
(53) Nguyen, S. T.; Nguyen, C. Q.; Hieu, N. N.; Phuc, H. V.; Nguyen, C. V. First-principles investigations of metal-semiconductor MoSH@MoS van der Waals heterostructures. *Nanoscale Adv.* **2023**, *5* (18), 4979−4985.
(54) Liu, Y. T.; Gao, T. H. First-principles study of controllable contact types in Janus MoSH/GaN van der Waals heterostructure. *J. Chem. Phys.* **2023**, *159* (9), No. 091101.
(55) Kresse, G.; Hafner, J. Ab initio molecular dynamics for liquid metals. *Phys. Rev. B Condens Matter* **1993**, *47* (1), 558−561.

https://doi.org/10.1021/acsomega.4c05356
ACS Omega 2024, 9, 48173−48184

(56) Kresse, G.; Furthmuller, J. Efficient iterative schemes for ab initio total-energy calculations using a plane-wave basis set. *Phys. Rev. B Condens Matter* **1996**, *54* (16), 11169−11186.
(57) Kresse, G.; Joubert, D. From ultrasoft pseudopotentials to the projector augmented-wave method. *Phys. Rev. B* **1999**, *59* (3), 1758−1775.
(58) Blöchl, P. E. Projector augmented-wave method. *Phys. Rev. B* **1994**, *50* (24), 17953−17979.
(59) Grimme, S.; Antony, J.; Ehrlich, S.; Krieg, H. A consistent and accurate ab initio parametrization of density functional dispersion correction (DFT-D) for the 94 elements H-Pu. *J. Chem. Phys.* **2010**, *132* (15), 154104.
(60) Monkhorst, H. J.; Pack, J. D. Special points for Brillouin-zone integrations. *Phys. Rev. B* **1976**, *13* (12), 5188−5192.
(61) Brandbyge, M.; Mozos, J.-L.; Ordejón, P.; Taylor, J.; Stokbro, K. Density-functional method for nonequilibrium electron transport. *Phys. Rev. B* **2002**, *65* (16), No. 165401.
(62) Henkelman, G.; Arnaldsson, A.; Jónsson, H. A fast and robust algorithm for Bader decomposition of charge density. *Comput. Mater. Sci.* **2006**, *36* (3), 354−360.
(63) Babar, V.; Sharma, S.; Shaikh, A. R.; Oliva, R.; Chawla, M.; Cavallo, L. Detecting Hachimoji DNA: An Eight-Building-Block Genetic System with MoS(2) and Janus MoSSe Monolayers. *ACS Appl. Mater. Interfaces* **2024**, *16* (17), 21427−21437.
(64) Chawla, M.; Kalra, K.; Cao, Z.; Cavallo, L.; Oliva, R. Occurrence and stability of anion-pi interactions between phosphate and nucleobases in functional RNA molecules. *Nucleic Acids Res.* **2022**, *50* (20), 11455−11469.
(65) Kalra, K.; Gorle, S.; Cavallo, L.; Oliva, R.; Chawla, M. Occurrence and stability of lone pair-pi and OH-pi interactions between water and nucleobases in functional RNAs. *Nucleic Acids Res.* **2020**, *48* (11), 5825−5838.
(66) Chawla, M.; Chermak, E.; Zhang, Q.; Bujnicki, J. M.; Oliva, R.; Cavallo, L. Occurrence and stability of lone pair-pi stacking interactions between ribose and nucleobases in functional RNAs. *Nucleic Acids Res.* **2017**, *45* (19), 11019−11032.
(67) Li, C. Z.; Sha, H.; Tao, N. J. Adsorbate effect on conductance quantization in metallic nanowires. *Phys. Rev. B* **1998**, *58* (11), 6775−6778.
(68) Li, C. Z.; He, H. X.; Bogozi, A.; Bunch, J. S.; Tao, N. J. Molecular detection based on conductance quantization of nanowires. *Appl. Phys. Lett.* **2000**, *76* (10), 1333−1335.
(69) Bogozi, A.; Lam, O.; He, H. X.; Li, C. Z.; Tao, N. J.; Nagahara, L. A.; Amlani, I.; Tsui, R. Molecular adsorption onto metallic quantum wires. *J. Am. Chem. Soc.* **2001**, *123* (19), 4585−4590.
(70) Jena, M. K.; Kumawat, R. L.; Pathak, B. First-Principles Density Functional Theory Study on Graphene and Borophene Nanopores for Individual Identification of DNA Nucleotides. *Acs Appl. Nano Mater.* **2021**, *4* (12), 13573−13586.
(71) Feliciano, G. T.; Sanz-Navarro, C.; Coutinho-Neto, M. D.; Ordejón, P.; Scheicher, R. H.; Rocha, A. R. Addressing the Environment Electrostatic Effect on Ballistic Electron Transport in Large Systems: A QM/MM-NEGF Approach. *J. Phys. Chem. B* **2018**, *122* (2), 485−492.
(72) Lagerqvist, J.; Zwolak, M.; Di Ventra, M. Influence of the environment and probes on rapid DNA sequencing via transverse electronic transport. *Biophys. J.* **2007**, *93* (7), 2384−2390.
(73) Kumawat, R. L.; Jena, M. K.; Mittal, S.; Pathak, B. Advancement of Next-Generation DNA Sequencing through Ionic Blockade and Transverse Tunneling Current Methods. *Small* **2024**, *20* (36), No. 2401112.

https://doi.org/10.1021/acsomega.4c05356
ACS Omega 2024, 9, 48173−48184